



Batteries Hot Paper

How to cite: *Angew. Chem. Int. Ed.* **2020**, 59, 12147–12153

International Edition: doi.org/10.1002/anie.202004284

German Edition: doi.org/10.1002/ange.202004284

# A Two-Dimensional Mesoporous Polypyrrole–Graphene Oxide Heterostructure as a Dual-Functional Ion Redistributor for Dendrite-Free Lithium Metal Anodes

Haodong Shi<sup>+</sup>, Jieqiong Qin<sup>+</sup>, Kai Huang, Pengfei Lu, Chuanfang (John) Zhang, Yanfeng Dong, Mao Ye, Zhongmin Liu, and Zhong-Shuai Wu\*

Dedicated to the 70th anniversary of the Dalian Institute of Chemical Physics, CAS

**Abstract:** Guiding the lithium ion (Li-ion) transport for homogeneous, dispersive distribution is crucial for dendrite-free Li anodes with high current density and long-term cyclability, but remains challenging for the unavailable well-designed nanostructures. Herein, we propose a two-dimensional (2D) heterostructure composed of defective graphene oxide (GO) clipped on mesoporous polypyrrole (mPPy) as a dual-functional Li-ion redistributor to regulate the stepwise Li-ion distribution and Li deposition for extremely stable, dendrite-free Li anodes. Owing to the synergy between the Li-ion transport nanochannels of mPPy and the Li-ion nanosieves of defective GO, the 2D mPPy-GO heterostructure achieves ultralong cycling stability (1000 cycles), even tests at 0 and 50°C, and an ultralow overpotential of 70 mV at a high current density of 10.0 mA cm<sup>-2</sup>, outperforming most reported Li anodes. Furthermore, mPPy-GO-Li/LiCoO<sub>2</sub> full batteries demonstrate remarkably enhanced performance with a capacity retention of >90% after 450 cycles. Therefore, this work opens many opportunities for creating 2D heterostructures for high-energy-density Li metal batteries.

## Introduction

With the ever-increasing global fossil energy crisis and environmental concerns regarding clean energy, developing high-energy-density batteries is becoming extremely critical to fulfill the long-range cruising requirements in high-end future applications, such as portable electronics and electric vehicles.<sup>[1]</sup> Although Li-ion batteries are the most popular power sources, their energy densities are approaching the theoretical limits. Alternatively, Li metal cells, such as Li-oxide and Li-sulfur batteries, are considered as next-generation high-energy-density secondary batteries owing to their high theoretical capacity (3860 mAh g<sup>-1</sup>) and low electrochemical potential (−3.04 V vs. SHE).<sup>[2]</sup> However, the poor

cycle lifetime, low cycling efficiency, and safety issues caused by nonuniform Li dendrites and large volume changes during Li plating/stripping substantially prevent the wide application of Li metal batteries.<sup>[3]</sup>

According to the widely accepted Sand's time model,<sup>[4]</sup> describing the initial nucleation process of growing Li dendrites, a small effective current density, a steady solid electrolyte interface (SEI), and a stable anionic ion transference number are the key factors to suppress Li dendrite formation.<sup>[5]</sup> Based on this theory, advanced approaches have been proposed and tested, including 1) designing 3D high-surface-area current collectors as skeletons to decrease the current density and minimize the volume changes for stable Li metal anodes;<sup>[6]</sup> 2) employing lithiophilic alloys (e.g., Li/Al, Li/Ag, Li/Si, Li/Na) as Li metal nucleation sites to govern uniform Li-ion diffusion;<sup>[7]</sup> and 3) engineering functional electrolyte additives (e.g., LiNO<sub>3</sub>, Cs<sup>+</sup>, Li<sub>2</sub>S<sub>8</sub>) for strengthening the SEI film or designing high-modulus solid electrolytes (e.g., inorganic, polymer, hybrid) to reduce the secondary reaction between anode and electrolyte for homogeneous Li deposition.<sup>[3a,8]</sup> However, these strategies are still not satisfying, for instance, the uneven growth of Li dendrites can hardly be fully hindered in the inner space of 3D hosts, the use of Li alloys is often limited by complex synthetic processes and a low Li content, and SEI-stabilized electrolyte additives are easily consumed as the cyclic proceeds, while solid-state electrolytes suffer from low ionic conductivities and increased polarization voltages, which has greatly limited the development of Li-metal batteries.<sup>[9]</sup>

To solve the intrinsic issues of Li-metal batteries described above, suppressing Li dendrites at a fundamental level is urgently required. Recently, nanoporous structures for uniform Li-ion flux on the electrolyte/electrode interface have been designed to effectively realize dendrite-free Li anodes. For instance, electrodes have been modified with either thin

[\*] H. Shi,<sup>[a]</sup> J. Qin,<sup>[a]</sup> K. Huang, Dr. P. Lu, Dr. Y. Dong, Prof. M. Ye, Prof. Z. M. Liu, Prof. Z.-S. Wu  
Dalian National Laboratory for Clean Energy  
Dalian Institute of Chemical Physics  
Chinese Academy of Sciences  
Dalian 116023 (P. R. China)  
E-mail: wuzs@dicp.ac.cn  
H. Shi,<sup>[a]</sup> J. Qin,<sup>[a]</sup> K. Huang  
University of Chinese Academy of Sciences  
Beijing 100049 (P. R. China)

Dr. C. Zhang  
Swiss Federal Laboratories for Materials Science and Technology  
Dübendorf (Switzerland)  
Dr. Y. Dong  
Northeastern University  
Shenyang 110819 (P. R. China)

[†] These authors contributed equally to this work.

Supporting information and the ORCID identification number(s) for the author(s) of this article can be found under:  
 <https://doi.org/10.1002/anie.202004284>.

polymer layers or vertically aligned nanochannels,<sup>[9a]</sup> and fast-ion-transport channel layers have been coated onto porous polypropylene separators.<sup>[10]</sup> In addition, 2D materials, such as GO or boron nitride, with abundant defect sites and high mechanical stability, have been proposed as nanoporous buffer layers for the uniform growth of metallic Li.<sup>[11]</sup> Despite great progress, the reasonable construction of an effective nanoporous architecture that is capable of regulating the uniformity of Li-ion plating at a high current density (e.g.,  $\geq 5 \text{ mA cm}^{-2}$ ) while maintaining long-term cycling lifetimes (e.g.,  $\geq 1000$  cycles) still remains challenging.<sup>[12]</sup>

Herein, we report the hard-template synthesis of a 2D heterostructure of mPPy uniformly grown on defective graphene oxide (mPPy-GO) to generate a new dual-functional Li-ion redistributor, which can homogenize Li-ion deposition for extremely stable and dendrite-free Li anodes. By taking advantage of the synergistic effects arising from the continuous Li-ion transport nanochannels of mPPy and the Li-ion nanosieves of defective GO nanosheets, homogeneous Li-ion fluxes are achieved. As a result, the mPPy-GO heterostructure electrode exhibits an impressive electrochemical performances, including a stable Coulombic efficiency of 98% coupled with flat voltage profiles (70 mV) at a high current density of  $10 \text{ mA cm}^{-2}$  and an ultralong cycling stability even under harsh conditions (0 and  $50^\circ\text{C}$ ). Finally, an impressive capacity retention of near 90% with an excellent Coulombic efficiency of almost 100% is recorded for the mPPy-GO-Li//LiCoO<sub>2</sub> full battery after 450 cycles.

## Results and Discussion

The synthesis of the 2D heterogeneous mPPy-GO nanosheets is illustrated in Figure 1a. First, functionalized GO nanosheets with positive charges and numerous defects (see the Supporting Information, Figure S1) were employed as 2D substrates, and electrostatically assembled with negatively charged monodisperse SiO<sub>2</sub> nanospheres (22 nm) to obtain SiO<sub>2</sub>-GO hybrids. Afterwards, using the SiO<sub>2</sub>-GO hybrids as 2D mesoporous templates, patterning of the homogeneous PPy layer was conducted to form SiO<sub>2</sub>-PPy-GO composites. Subsequently, mPPy-GO nanosheets with defined mesopores were obtained after etching of the SiO<sub>2</sub> templates. The resulting mPPy-GO nanosheets had a uniform, flat, sheet-like morphology with a thickness of about 43 nm (Figure 1b,c).

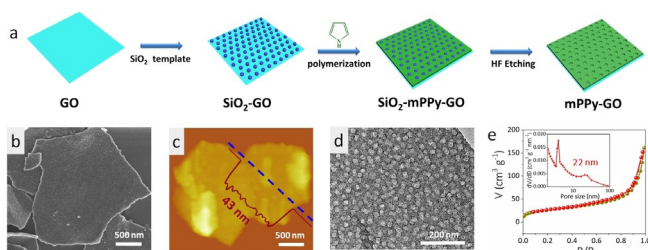


**Figure 1.** Schematic illustration and characterization of the 2D mPPy-GO heterostructure. a) Fabrication of the 2D mPPy-GO heterostructure. b) SEM image, c) AFM image and height profile, d) TEM image, and e) N<sub>2</sub> adsorption-desorption isotherm of the 2D mPPy-GO heterostructure. The inset in (e) is a plot of the pore size distribution.

Enriched arrays of mesopores with a uniform size of ca. 22 nm were patterned on the top and bottom surfaces of defective GO (Figure 1d and Figures S2, S3). The N<sub>2</sub> adsorption/desorption isotherm revealed a BET specific surface area of  $94 \text{ m}^2 \text{ g}^{-1}$  in the mPPy-GO nanosheets, and confirmed the presence of mesopores with a size of about 22 nm (Figure 1e). A Raman spectrum and a Fourier transform IR (FTIR) spectrum showed the uniform and compact integration of the GO and mPPy components (Figures S4, S5).<sup>[13]</sup>

To investigate the superior electrochemical performance of the 2D mPPy-GO heterostructure, half-cells were assembled by pairing Li foil with mPPy-GO electrodes. For comparison, nonporous PPy-GO (Figure S6), pure GO (Figure S7), graphene, and bare Cu electrode based half cells were also fabricated. The cells were firstly cycled between 0.01 and 1 V for 5 cycles to form a stable SEI film (Figure S8). During each discharge/charge cycle with a Li deposition capacity of  $0.5 \text{ mAh cm}^{-2}$  at  $0.5 \text{ mA cm}^{-2}$ , the mPPy-GO electrode showed highly stable Coulombic efficiencies of 99% (145th cycle), which are significantly higher than those of nonporous PPy-GO (86% for the 105th cycle), GO (93% for the 92th cycle), PPy (89% for the 81th cycle), graphene (76% for the 92th cycle), and Cu (86% for the 78th cycle) electrodes (Figure 2a). The superiority of the mPPy-GO electrodes was more prominent when an increased amount of  $1 \text{ mAh cm}^{-2}$  of Li was plated and stripped in each cycle (Figure 2b). In addition, after establishing a stable interface between the electrolyte and the electrode in the early cycles, the mPPy-GO electrodes maintained higher Coulombic efficiencies and better cycling stabilities than bare Cu electrodes even at a higher current density ( $1 \text{ mA cm}^{-2}$ ; Figure S9a,b) or for a larger amount of deposited Li (Figure S9c,d), confirming the synergistic Li-ion redistribution effect of mPPy and defective GO in the mPPy-GO heterostructure. Furthermore, their electrochemical stabilities were also tested under harsh conditions, namely at 0 and  $50^\circ\text{C}$ . At  $0^\circ\text{C}$ , the mPPy-GO-Li electrode displayed a stable cycle performance over more than 50 cycles, while the bare Cu anode revealed a deteriorating cycle performance due to the slow electrochemical dynamics (Figure 2c and Figure S10). At  $50^\circ\text{C}$ , side reactions such as electrolyte decomposition and Li dendrite formation accelerated the deterioration of the cell cycle ability. Surprisingly, our mPPy-GO electrode showed an impressively stable Coulombic efficiency of 98.5% after 290 cycles, and is thus much more stable than bare Cu electrodes ( $< 90\%$  after 70 cycles, Figure 2d and Figure S11), obviously demonstrating the unique role of mPPy-GO in regulating the uniform Li flux for stable Li deposition.

The rate capability of the mPPy-GO electrode was also examined in comparison with that of bare Cu with an increased Li plating capacity at  $0.5 \text{ mA cm}^{-2}$ . The mPPy-GO electrode retained a high Coulombic efficiency of 99.5% when the Li deposition capacity reached up to  $6 \text{ mAh cm}^{-2}$  for more than 70 cycles, while the bare Cu electrode quickly failed at a capacity of  $\geq 0.5 \text{ mAh cm}^{-2}$  (Figure 2e). Moreover, the Coulombic efficiency of mPPy-GO at increased current densities from 0.25 to  $2.5 \text{ mA cm}^{-2}$  for the same plating time of 1 h always exceeded 97% during the entire cycles, while that of the Cu electrode quickly decreased as the current

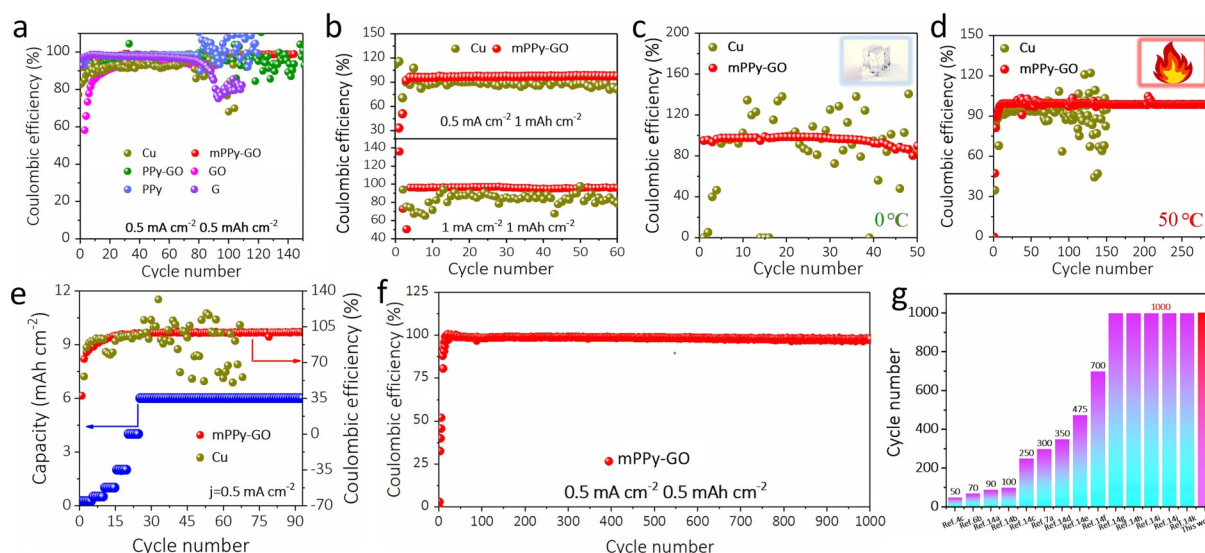


**Figure 2.** Coulombic efficiency of 2D mPPy-GO heterostructure electrodes. a) The Coulombic efficiencies of 2D mPPy-GO, PPy-GO, GO, graphene (G), pure PPy, and Cu electrodes with a Li deposition of  $0.5 \text{ mAh cm}^{-2}$  at  $0.5 \text{ mA cm}^{-2}$ . b) The Coulombic efficiencies of 2D mPPy-GO electrodes compared to those of Cu electrodes at  $0.5 \text{ mA cm}^{-2}$  (top) and  $1 \text{ mA cm}^{-2}$  (bottom) with  $1 \text{ mAh cm}^{-2}$  cycling capacity. c, d) The Coulombic efficiencies of mPPy-GO and Cu electrodes at c) a low temperature of  $0^\circ\text{C}$ , and d) a high temperature of  $50^\circ\text{C}$  with a Li deposition of  $0.5 \text{ mAh cm}^{-2}$  at  $0.5 \text{ mA cm}^{-2}$ . e) Coulombic efficiencies of mPPy-GO and controlled Cu electrodes with increasing capacities at a fixed current density of  $0.5 \text{ mA cm}^{-2}$ . f) Ultralong Coulombic efficiency test of the mPPy-GO electrode with a capacity of  $0.5 \text{ mAh cm}^{-2}$  at  $0.5 \text{ mA cm}^{-2}$ . g) Cycle number of mPPy-GO electrode tested at a current density of  $0.5 \text{ mA cm}^{-2}$ , compared with those of previously reported cells with Li-metal anodes stabilized by various strategies.

density increased beyond  $0.5 \text{ mAh cm}^{-2}$  (Figure S12), indicating the greatly enhanced Li-ion transport kinetics of the mPPy-GO heterostructure. Indeed, our mPPy-GO electrode was capable of maintaining high/stable Coulombic efficiencies over ultralong cycles (ca. 98.2% over 1000 cycles for 2000 h; Figure 2f), rendering it superior in this aspect to most of the Li-metal anodes stabilized by various strategies (Figure 2g, Table S1),<sup>[4c,6b,7a,14]</sup> such as unstacked graphene (93% for 50 cycles),<sup>[4c]</sup> 3D Cu (97% for 70 cycles),<sup>[6b]</sup> and hollow carbon (98% for 300 cycles).<sup>[7a]</sup>

Electrolyte wettability is key to influence the distribution of Li ions in the electrode, which plays a critical role in the growth of metallic Li dendrites.<sup>[15]</sup> Once the electrolyte was dropped on mPPy-GO, the electrode was immediately wetted and almost permeated within 30 s (with a negligible contact angle of  $4.8^\circ$ ; Figure 3a, top). In contrast, the electrolyte droplet still stood on the surface of a Cu layer even after 1 min (with a contact angle of  $24.5^\circ$ ; Figure 3a, bottom). Further, density functional theory (DFT) calculations confirmed that the formation energy of Li-ion adsorption on the Li(100) surface in the presence of electrolyte was higher than that without electrolyte ( $\Delta E = 0.08 \text{ eV}$ ; Figure 3b). As a result, the mPPy-GO electrode with superior electrolyte wettability is favorable for the uniform deposition of Li metal on the framework. Moreover, the outstanding electrolyte wettability could facilitate the nucleation of Li at low overpotentials (Figure 3c). For instance, the plating overpotential (reflecting the difficulty of metallic Li nucleation) was about  $0.2 \text{ V}$  in the bare Cu electrode, but sharply decreased to  $0.08 \text{ V}$  in the mPPy-GO electrode, indicating the exceptional lithiophilicity in the latter. Consequently, stable Li plating/stripping profiles with a smaller voltage hysteresis ( $18 \text{ mV}$ ) was achieved on the

mPPy-GO electrode, in sharp contrast to the large and fluctuant voltage hysteresis on the bare Cu electrode (Figure S13).

The greatly enhanced long-term Li cycling stability can be attributed to the differences in forming/stabilizing the SEI film.<sup>[16]</sup> Unlike the mPPy-GO electrode, the bare Cu electrode is non-lithiophilic, and free of interconnected mesoporous channels. As a result, the SEI film is continuously formed/damaged and thus keeps consuming the electrolyte. To further highlight the crucial influence of SEI formation on suppressing Li dendrite formation, we studied the Coulombic efficiency of two electrodes between 0.01 and 3 V vs. Li/Li<sup>+</sup>. Galvanostatic results indicated that the mPPy-GO electrode showed an initial Coulombic efficiency of 83%, which quickly stabilized at a high Coulombic efficiency of 94% after four cycles (Figure 3d, top). In sharp contrast, the cycling Coulombic efficiency of bare Cu was always below 45% in the first four cycles (Figure 3d, bottom). The different stabilities of the SEI layers were further confirmed by in situ electrochemical impedance spectroscopy (EIS) at different cycling states (i–vi: corresponding to different Li deposition areal capacities, Figure S14). Impressively, the mPPy-GO electrode not only exhibited a smaller charge transfer resistance ( $R_{\text{ct}}$ , reflecting the SEI-related surface film impedance; Figure 3e, Figure S15), but also maintained a relatively stable value at the different cycling states compared with bare Cu, which further confirmed the greater stability of the SEI layer of the mPPy-GO electrode (Figure 3f, g and Table S2). Moreover, the slope of the mPPy-GO electrode was much smaller than that of a pure Cu electrode at low frequency (Figure S16), indicating the excellent Li-ion diffusion performance of the mPPy-GO electrode.<sup>[17]</sup> To reveal the SEI composition on the

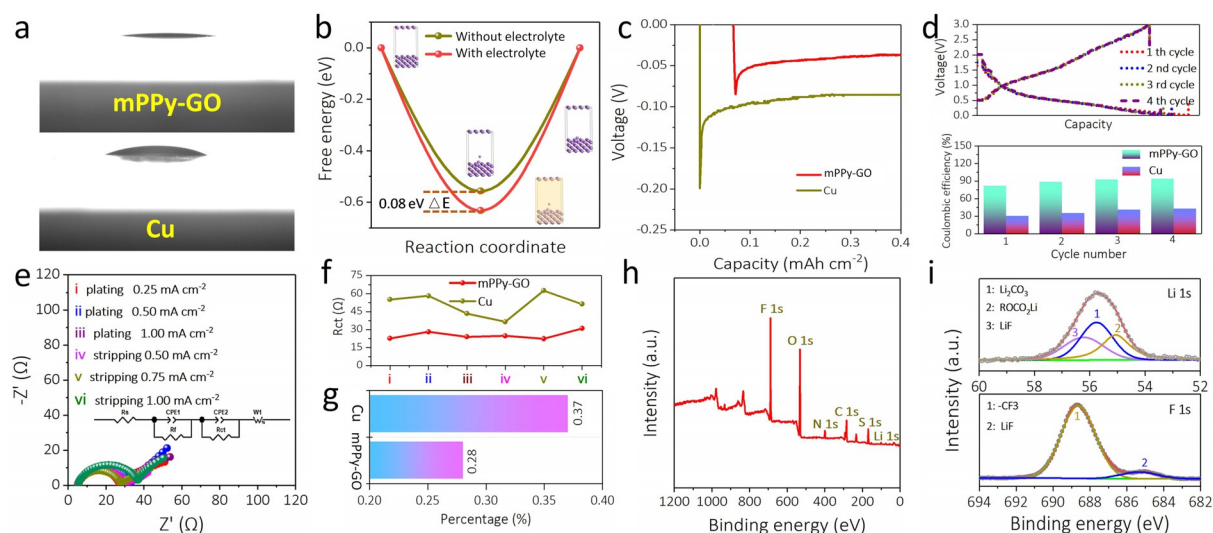


**Figure 3.** Superior electrolyte wettability and stable SEI layer of 2D mPPy-GO heterostructure electrodes. a) Contact angle of an organic electrolyte drop on mPPy-GO (top) and Cu electrodes (bottom). b) Free energy curves of electrode with and without electrolyte. c) Nucleation section on the voltage profiles of mPPy-GO and Cu electrodes in the first cycle. d) Charge–discharge behavior of an mPPy-GO electrode tested in a voltage range of 0.01–3 V at 100 mA in the first four cycles (top) and the corresponding Coulombic efficiencies of mPPy-GO and Cu electrodes (bottom). e) Nyquist plots of mPPy-GO electrodes at different cycling stages. f) The variation and g) corresponding change rate of  $R_{ct}$  at different stages from (i) to (vi) in (e). h) XPS full spectrum and i) Li 1s (top) and F 1s (bottom) XPS spectra of the mPPy-GO electrode after 10 cycles.

cycled Li metal, X-ray photoelectron spectroscopy (XPS) was employed, showing the presence of inorganic Li salts, such as  $\text{Li}_2\text{CO}_3$ ,  $\text{ROCO}_2\text{Li}$ , and  $\text{LiF}$  (Figure 3h,i and Figure S17).<sup>[18]</sup> We note that the formation of stable SEI layers is crucial for inhibiting the growth of Li dendrites and improving the stability of the Li-metal anode, as described below.

Symmetric cells based on mPPy-GO-Li/mPPy-GO-Li, PPy-GO-Li/PPy-GO-Li, GO-Li/GO-Li, and Cu-Li/Cu-Li were assembled to measure the voltage hysteresis and cycling stability. With a deposition capacity of  $1 \text{ mAh cm}^{-2}$  at  $1 \text{ mA cm}^{-2}$ , mPPy-GO-Li cells exhibited flat and consistent voltage profiles with a small hysteresis of 9 mV for more than 1100 h without short circuit (Figure 4a,b and Figure S18). In contrast, for Cu-Li, PPy-GO-Li, and GO-Li based symmetric cells, the overpotential considerably increased after 135, 550, and 745 h with a fluctuant voltage hysteresis of around 40, 75, and 41 mV, respectively, coupled with a noisy voltage hysteresis and abrupt voltage changes upon cycling for different periods of time (Figure 4c–f). Even with the highly active carbonate-based electrolyte, the mPPy-GO-Li cells could still realize a stable voltage hysteresis of 50 mV for more than 700 h (Figure S19). The instability of voltage hysteresis could be fairly attributed to the short circuit caused by inhomogeneous Li distribution.<sup>[14c]</sup> Furthermore, at an increased current density ( $5 \text{ mA cm}^{-2}$ ), mPPy-GO-Li cells delivered an overpotential of only about 22 mV and a stable cycling stability beyond 400 h, while the bare Cu-Li cells failed with substantial voltage fluctuation at 65 h ( $> 290 \text{ mV}$ ; Figure 4g). Upon increasing the current density up to  $10 \text{ mA cm}^{-2}$  at a higher capacity ( $5 \text{ mAh cm}^{-2}$ ), steady hysteresis (70 mV) was also attained after 100 cycles for mPPy-GO-Li cells, further confirming the advantages of 2D heterostructures in generating long-term-cycling electrodes with low, steady voltage hysteresis (Figure S20). When the rate capability of mPPy-GO-Li cells was tested at increased

current densities for 0.5 h, the voltage hysteresis increased from 4 to 35 mV as the current density was increased from 0.25 to  $10 \text{ mA cm}^{-2}$ . However, the bare Li electrode succumbed to severe voltage fluctuation even at a current density of  $3 \text{ mA cm}^{-2}$  (Figure 4h). It should be emphasized that the

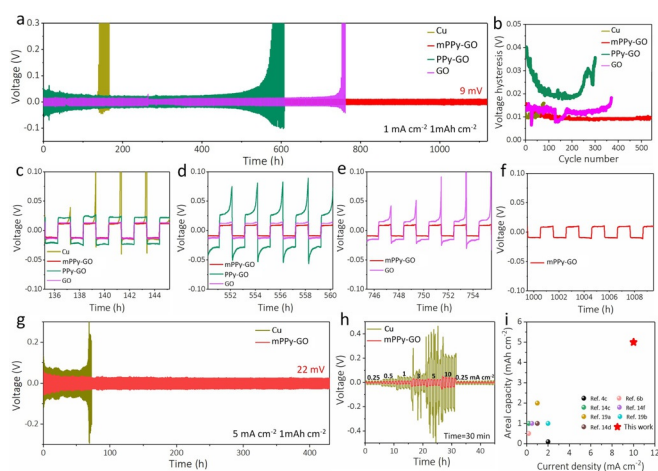


**Figure 4.** Electrochemical performance of symmetric cells with 2D mPPy-GO heterostructure anodes. a) Galvanostatic cycling of symmetric cells based on mPPy-GO-Li, PPy-GO-Li, GO-Li, and Cu-Li anodes with a current density of  $1 \text{ mA cm}^{-2}$  at a stripping/plating capacity of  $1 \text{ mAh cm}^{-2}$ . b) Corresponding voltage hysteresis variation with cycle number. c–f) Magnified Li plating/stripping profiles for the cycling periods c) 135–145 h, d) 550–560 h, e) 745–755 h, and f) 1000–1110 h. g) High current density ( $5 \text{ mA cm}^{-2}$ ) cycling of symmetric cells based on mPPy-GO-Li and bare Cu-Li anodes with a capacity of  $1 \text{ mAh cm}^{-2}$ . h) Rate capability of mPPy-GO-Li and bare Cu-Li cells obtained at different current densities of 0.25, 0.5, 1, 3, 5, and  $10 \text{ mA cm}^{-2}$  for 30 min in both the Li-stripping and Li-plating processes of each cycle. i) Comparison of the gravimetric capacity vs. current density of the mPPy-GO-Li anode with currently reported Li composite anodes and pure Li/LCO cells.

ultrahigh cycle rate of  $10 \text{ mA cm}^{-2}$  coupled with a high capacity of  $5 \text{ mAh cm}^{-2}$  of our mPPy-GO-Li anode has outperformed most other reported composite Li-metal anodes (Figure 4i),<sup>[4c, 6a, b, 14c, d, 19]</sup> such as 3D Cu ( $0.2 \text{ mA cm}^{-2}$ ,  $0.5 \text{ mAh cm}^{-2}$ ),<sup>[6b]</sup> 3D porous Cu ( $0.2 \text{ mA cm}^{-2}$ ,  $1 \text{ mAh cm}^{-2}$ ),<sup>[14c]</sup> and graphitized carbon fiber ( $2 \text{ mA cm}^{-2}$ ,  $1 \text{ mAh cm}^{-2}$ ).<sup>[19b]</sup> Correspondingly, the EIS measurements also confirmed the lower polarization and reduced  $R_{ct}$  value of only  $6.8 \Omega$  compared to Cu-Li ( $18 \Omega$ ), indicating much enhanced Li ionic transport kinetics and improved cyclability in mPPy-GO heterostructures (Figure S21).

To further confirm the dual-functional Li-ion redistribution in the 2D mPPy-GO heterostructures for promoting dendrite-free Li deposition during cycling, DFT simulations were performed. Compared with bare Cu foil, a more homogeneous Li deposition after 1.00 ns was found for a Cu foil with the buffer layer. We surmise that the mechanically stable and flexible GO protective films can act as physical barriers to delay the transfer of Li ions, and prevent the “tip effect” due to the intrinsic defect sites of GO (Figure 5a, b).<sup>[11a, 20]</sup> Further, the distribution behavior of Li ions through 2D mPPy was simulated (Figure 5c), where Li ions could move along in the y axis direction (Figure S22) driven by the vertical electric field. Notably, the mesopores in the PPy layer were the only pathway for Li-ion migration. Based on finite volume method (FVM) results (Figure 5d, e), with the staggered arrangement of mesopores in PPy, the distribution of Li ions become more uniform as Li ions migrate along the y axis, contributing to a homogeneous Li distribution. Compared with bare Cu, where Li ions are easily trapped to form “tip effects” and induce Li dendrites, the 2D mPPy-GO heterostructure could act as a dual-functional redistributor to exceptionally dissipate the concentrated Li ions for realizing uniform Li-ion distribution and smooth Li deposition (Figure 5f).

The morphology change of conductive mPPy-GO anodes (ca.  $7.5 \text{ S cm}^{-1}$ ) after Li plating/stripping was systematically studied (Figure 5g–j and Figure S23). After electroplating Li metal for 0.5 h ( $0.25 \text{ mAh cm}^{-2}$ ), top-view and cross-sectional scanning electron microscopy (SEM) images of the mPPy-GO electrode showed uniform and dense nanosheet-stacked structures with a thickness of approximately  $22.9 \mu\text{m}$  (Figure 5g and Figure S24a). Increasing the Li plating capacity to 0.5 and  $1 \text{ mAh cm}^{-2}$  led to complete and uniform coverage with dense Li ( $25.0 \mu\text{m}$ ) of the mPPy-GO electrode. No apparent Li dendrites were found (Figure 5h, i and Figure S24b, c), indicating that a dendrite-free Li plating process had been achieved in the mPPy-GO electrode. Moreover, the mPPy-GO electrode skeleton could be fully recovered after Li stripping with almost unchanged scaffold thickness (Figure 5j and Figure S24d). On the contrary, bare Cu electrodes at different plating/stripping states showed mossy surfaces with a big fluctuation in thickness, suggestive of large volume changes caused by the significant formation of dendrites (Figures S25, S26).<sup>[21]</sup>

To highlight the practical application of 2D mPPy-GO-Li anodes, three full cells were assembled by pairing a LiCoO<sub>2</sub> (LCO) cathode with mPPy-GO-Li, pure Li foil, and Cu-Li anodes ( $5 \text{ mAh cm}^{-2}$ ), respectively. We first tested the cycling

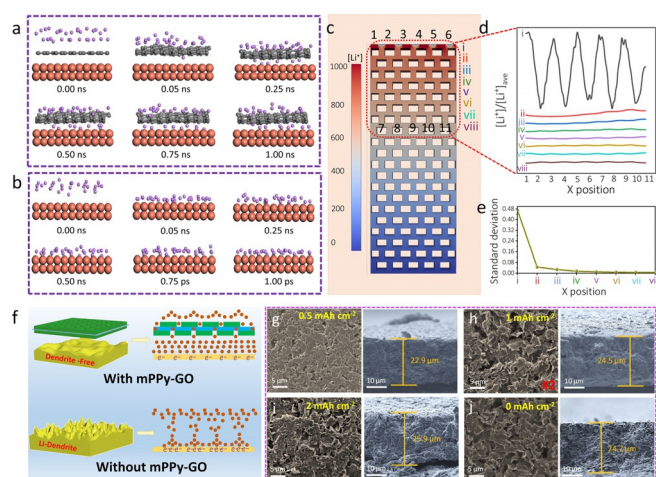


**Figure 5.** Li-ion transportation behaviors of the 2D mPPy-GO heterostructure as dual-functional ion redistributor. a, b) Atomic configurations of the diffusion pathway of Li atoms on the Cu current collector a) with or b) without defective GO at different times. c) Distributions of Li ions through a 2D mPPy-GO heterostructure layer. The colors in the graph represent the concentration of Li ions ( $[\text{Li}^+]$ ). d) The relative concentration of Li ions and e) standard deviation of  $[\text{Li}^+]/[\text{Li}^+]_{\text{ave}}$  beneath the mPPy-GO layer at different thicknesses (i–viii) in the FEM simulation results.  $[\text{Li}^+]_{\text{ave}}$  is the average concentration of Li ions at each thickness. f) Schematic illustration of the electrochemical deposition behaviors of electrodes with 2D mPPy-GO heterostructures as dual-functional Li-ion redistributors for uniform Li deposition (top), and bare Cu (bottom). g–j) SEM images showing top views (left) and cross-sections (right) of mPPy-GO-Li electrodes during g) plating with a capacity of  $0.25 \text{ mAh cm}^{-2}$ , h) plating with a capacity of  $0.5 \text{ mAh cm}^{-2}$ , i) plating with a capacity of  $1 \text{ mAh cm}^{-2}$ , and j) stripping with a capacity of  $1 \text{ mAh cm}^{-2}$ .

performance of the full cells at 1 C. Notably, the discharge capacity of mPPy-GO-Li was  $141 \text{ mAh g}^{-1}$ , which is higher than those of pure Li ( $133 \text{ mAh g}^{-1}$ ) and Cu-Li ( $121 \text{ mAh g}^{-1}$ ) in the initial cycles. After cycling for 450 cycles, the capacity of pure Li/LCO cell decreased to only  $63 \text{ mAh g}^{-1}$ , showing a low capacity retention of 47%, and the bare Cu-Li only maintained  $16 \text{ mAh g}^{-1}$ , corresponding to 13% of the initial capacity. Inversely, a high discharge capacity of  $130 \text{ mAh g}^{-1}$ , about 92% of capacity retention, and outstanding cycling stability were achieved for the mPPy-GO-Li/LCO cell after the same cycling process (Figure 6a–c and Figure S27). Such a full cell could readily power 42 light-emitting diode (LED) arrays of the letters “DICP” for more than 0.5 h. Importantly, the Coulombic efficiency of the mPPy-GO-Li/LCO cell remained nearly 100% during cycling, while that of the Cu-Li cell showed large fluctuations (Figure 6d). Furthermore, the mPPy-GO-Li/LCO battery delivered a greatly enhanced rate capability, for instance,  $118 \text{ mAh g}^{-1}$  at 2 C and  $101 \text{ mAh g}^{-1}$  at 5 C for mPPy-GO-Li/LCO cells, while those of pure Li/LCO were 107 and  $88 \text{ mAh g}^{-1}$ , and those of Cu-Li/LCO were only 45 and  $5 \text{ mAh g}^{-1}$  at 2 C and 5 C, respectively (Figure 6e, f). In addition, the polarization during the charge and discharge plateaus for the mPPy-GO-Li/LCO battery ( $94 \text{ mV}$ ) was much smaller than for Li/LCO ( $123 \text{ mV}$ ) and Cu-Li/LCO cells ( $350 \text{ mV}$ ), demonstrating the significantly improved kinetics in the mPPy-GO-Li/LCO cell (Figure 6g).<sup>[22]</sup>

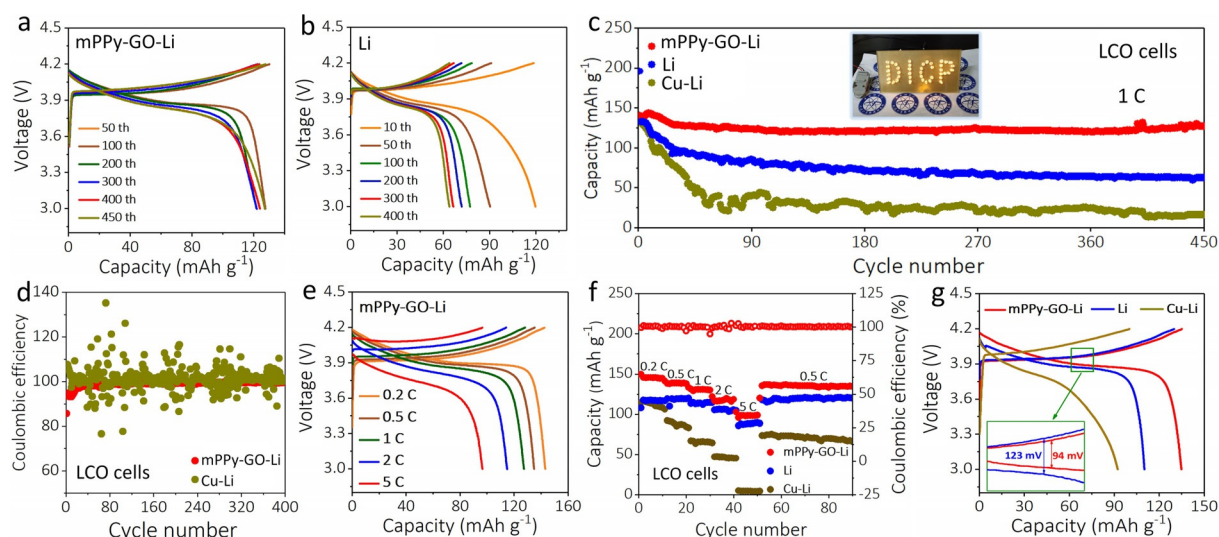


**Figure 6.** Electrochemical performance of Li/LCO full cells with different Li-metal anodes. a, b) Charge and discharge curves of a) mPPy-GO-Li/LCO and b) pure Li/LCO cells measured at 1 C for different cycles. c) Long-term cycling stability of full batteries based on mPPy-GO-Li, pure Li, and Cu-Li anodes with LCO cathodes tested at 1 C. d) Coulombic efficiencies of mPPy-GO-Li/LCO and Cu-Li/LCO cells at 1 C. e) Charge and discharge curves of mPPy-GO-Li/LCO cells obtained at a rate from 0.2 to 5 C. f) Rate capabilities of mPPy-GO-Li/LCO, pure Li/LCO, and Cu-Li/LCO cells obtained from 0.2 to 5 C. g) Voltage profile comparison of mPPy-GO-Li/LCO, pure Li/LCO, and Cu-Li/LCO cells obtained at 0.5 C. The inset shows the hysteresis of the mPPy-GO-Li/LCO cell.

The 2D mPPy-GO heterostructure has been demonstrated as a novel dual-functional Li-ion redistributor for exceptionally stable and dendrite-free Li anodes. The outstanding performance is attributed to the synergy in the 2D mPPy-GO heterostructure. First, the defective GO serving as a Li-ion nanosieve could sufficiently slow down the shuttling speed of Li ions between electrode and electrolyte, and reduce the Li dendrite growth rate, especially at high current densities (Figure 5a). Second, the highly ordered mesoporous arrays of the mPPy layer, providing abundant Li-ion-conducting nanochannels (Figure 5c–e), significantly lower the local effective current density and form a uniform Li-ion flux. Third, the excellent electrolyte wettability, high mechanical intensity, and outstanding chemical and physical stability of the 2D mPPy-GO heterostructure sufficiently enhance the strength of the uniform SEI film to prevent Li metal from the successive corrosion by the electrolyte. Consequently, the formation of Li dendrites and “dead Li” is eventually suppressed.

## Conclusion

In summary, a novel 2D heterostructure dual-functional Li-ion redistributor has been demonstrated to achieve homogenous Li-ion distribution for highly stable and dendrite-free Li metal anodes. Based on the synergy between the highly ordered Li-ion nanochannels of the 2D mesoporous mPPy layers and the nanosieves of the defective GO nanosheets, uniformly dispersed Li flux and remarkably reduced effective current densities were attained. The mPPy-GO electrode displayed a high Coulombic efficiency (98%) for up to 1000 cycles (2000 h), and flat voltage profiles (70 mV) at a high current density ( $10.0 \text{ mA cm}^{-2}$ ), coupled with long cyclability without dendrite growth even in extreme environ-

ments. Moreover, mPPy-GO-Li/LCO batteries showed significantly improved kinetics and capacity. Therefore, this new strategy for solving Li dendrite formation by making use of dual-functional 2D Li-ion redistributors will inspire the design and construction of Li-metal anodes toward high-energy-density Li batteries and other metal (Na, K, Zn) rechargeable batteries.

## Acknowledgements

This work was financially supported by the National Key R&D Program of China (Grant 2016YBF0100100), the National Natural Science Foundation of China (Grants 51572259, 51872283, and 21805273), the Liaoning Revitalization Talents Program (Grant XLYC1807153), the Natural Science Foundation of Liaoning Province (Grant 20180510038), DICP (DICP ZZBS201708, DICP ZZBS201802), DICP&QIBEBT (Grant DICP&QIBEBT UN201702), the Dalian National Laboratory For Clean Energy (DNL), CAS, and the DNL Cooperation Fund, CAS (DNL180310, DNL180308, DNL201912, and DNL201915).

## Conflict of interest

The authors declare no conflict of interest.

**Keywords:** graphene oxide · heterostructures · lithium metal anodes · mesoporous materials · polypyrrole

- [1] a) K. Kang, Y. S. Meng, J. Bréger, C. P. Grey, G. Ceder, *Science* **2006**, *311*, 977–980; b) M. Armand, J.-M. Tarascon, *Nature* **2008**, *451*, 652–657; c) R. Schmich, R. Wagner, G. Hörpel, T. Placke, M. Winter, *Nat. Energy* **2018**, *3*, 267–278; d) G. Assat, J.-M. Tarascon, *Nat. Energy* **2018**, *3*, 373–386.
- [2] a) X.-B. Cheng, R. Zhang, C.-Z. Zhao, Q. Zhang, *Chem. Rev.* **2017**, *117*, 10403–10473; b) R. Younesi, G. M. Veith, P. Johansson, K. Edström, T. Vegge, *Energy Environ. Sci.* **2015**, *8*, 1905–1922; c) P. G. Bruce, S. A. Freunberger, L. J. Hardwick, J.-M. Tarascon, *Nat. Mater.* **2012**, *11*, 19–29; d) X. Y. Yang, X. L. Feng, X. Jin, M. Z. Shao, B. L. Yan, J. M. Yan, Y. Zhang, X. B. Zhang, *Angew. Chem. Int. Ed.* **2019**, *58*, 16411–16415; *Angew. Chem.* **2019**, *131*, 16563–16567.
- [3] a) J. Zheng, M. H. Engelhard, D. Mei, S. Jiao, B. J. Polzin, J.-G. Zhang, W. Xu, *Nat. Energy* **2017**, *2*, 1–8; b) D. Lin, Y. Liu, Y. Cui, *Nat. Nanotechnol.* **2017**, *12*, 194–206; c) W. Xu, J. Wang, F. Ding, X. Chen, E. Nasybulin, Y. Zhang, J.-G. Zhang, *Energy Environ. Sci.* **2014**, *7*, 513–537.
- [4] a) V. Fleury, J.-N. Chazalviel, M. Rosso, B. Sapoval, *J. Electroanal. Chem. Interfacial Electrochem.* **1990**, *290*, 249–255; b) J.-N. Chazalviel, *Phys. Rev. A* **1990**, *42*, 7355; c) R. Zhang, X. B. Cheng, C. Z. Zhao, H. J. Peng, J. L. Shi, J. Q. Huang, J. Wang, F. Wei, Q. Zhang, *Adv. Mater.* **2016**, *28*, 2155–2162; d) C. Brissot, M. Rosso, J.-N. Chazalviel, P. Baudry, S. Lascaud, *Electrochim. Acta* **1998**, *43*, 1569–1574.
- [5] a) S. Jin, Z. Sun, Y. Guo, Z. Qi, C. Guo, X. Kong, Y. Zhu, H. Ji, *Adv. Mater.* **2017**, *29*, 1700783; b) L. Li, S. Li, Y. Lu, *Chem. Commun.* **2018**, *54*, 6648–6661; c) W. Deng, X. Zhou, Q. Fang, Z. Liu, *Adv. Energy Mater.* **2018**, *8*, 1703152.
- [6] a) Z. Sun, S. Jin, H. Jin, Z. Du, Y. Zhu, A. Cao, H. Ji, L. J. Wan, *Adv. Mater.* **2018**, *30*, 1800884; b) C.-P. Yang, Y.-X. Yin, S.-F. Zhang, N.-W. Li, Y.-G. Guo, *Nat. Commun.* **2015**, *6*, 8058; c) Y. Liu, D. Lin, Z. Liang, J. Zhao, K. Yan, Y. Cui, *Nat. Commun.* **2016**, *7*, 10992.
- [7] a) K. Yan, Z. Lu, H.-W. Lee, F. Xiong, P.-C. Hsu, Y. Li, J. Zhao, S. Chu, Y. Cui, *Nat. Energy* **2016**, *1*, 16010; b) X. Liang, Q. Pang, I. R. Kochetkov, M. S. Sempere, H. Huang, X. Sun, L. F. Nazar, *Nat. Energy* **2017**, *2*, 17119; c) J. L. Ma, F. L. Meng, Y. Yu, D. P. Liu, J. M. Yan, Y. Zhang, X. B. Zhang, Q. Jiang, *Nat. Chem.* **2019**, *11*, 64–70.
- [8] a) W. Li, H. Yao, K. Yan, G. Zheng, Z. Liang, Y.-M. Chiang, Y. Cui, *Nat. Commun.* **2015**, *6*, 7436; b) D. J. Yoo, K. J. Kim, J. W. Choi, *Adv. Energy Mater.* **2018**, *8*, 1702744; c) X. B. Cheng, R. Zhang, C. Z. Zhao, F. Wei, J. G. Zhang, Q. Zhang, *Adv. Sci.* **2016**, *3*, 1500213; d) H. Duan, Y.-X. Yin, Y. Shi, P.-F. Wang, X.-D. Zhang, C.-P. Yang, J.-L. Shi, R. Wen, Y.-G. Guo, L.-J. Wan, *J. Am. Chem. Soc.* **2018**, *140*, 82–85; e) Y. Yu, X.-B. Zhang, *Matter.* **2019**, *1*, 881–892; f) Y. Yu, Y.-B. Yin, J.-L. Ma, Z.-W. Chang, T. Sun, Y.-H. Zhu, X.-Y. Yang, T. Liu, X.-B. Zhang, *Energy Storage Mater.* **2019**, *18*, 382–388; g) H. Chu, H. Noh, Y. J. Kim, S. Yuk, J. H. Lee, J. Lee, H. Kwack, Y. Kim, D. K. Yang, H. T. Kim, *Nat. Commun.* **2019**, *10*, 188.
- [9] a) W. Liu, D. Lin, A. Pei, Y. Cui, *J. Am. Chem. Soc.* **2016**, *138*, 15443–15450; b) B. Liu, J.-G. Zhang, W. Xu, *Joule* **2018**, *2*, 833–845; c) H. Yang, C. Guo, A. Naveed, J. Lei, J. Yang, Y. Nuli, J. Wang, *Energy Storage Mater.* **2018**, *14*, 199–221; d) Y. Gu, W.-W. Wang, Y.-J. Li, Q.-H. Wu, S. Tang, J.-W. Yan, M.-S. Zheng, D.-Y. Wu, C.-H. Fan, W.-Q. Hu, *Nat. Commun.* **2018**, *9*, 1339.
- [10] C.-Z. Zhao, P.-Y. Chen, R. Zhang, X. Chen, B.-Q. Li, X.-Q. Zhang, X.-B. Cheng, Q. Zhang, *Sci. Adv.* **2018**, *4*, eaat3446.
- [11] a) T. Foroozan, F. A. Soto, V. Yurkiv, S. Sharifi-Asl, R. Deivanayagam, Z. Huang, R. Rojaee, F. Mashayek, P. B. Balbuena, R. Shahbazian-Yassar, *Adv. Funct. Mater.* **2018**, *28*, 1705917; b) K. Yan, H.-W. Lee, T. Gao, G. Zheng, H. Yao, H. Wang, Z. Lu, Y. Zhou, Z. Liang, Z. Liu, *Nano Lett.* **2014**, *14*, 6016–6022.
- [12] K. Zhang, G. H. Lee, M. Park, W. Li, Y. M. Kang, *Adv. Energy Mater.* **2016**, *6*, 1600811.
- [13] a) H. Zhou, G. Han, Y. Xiao, Y. Chang, H.-J. Zhai, *J. Power Sources* **2014**, *263*, 259–267; b) T. Qian, S. Wu, J. Shen, *Chem. Commun.* **2013**, *49*, 4610–4612.
- [14] a) X. B. Cheng, T. Z. Hou, R. Zhang, H. J. Peng, C. Z. Zhao, J. Q. Huang, Q. Zhang, *Adv. Mater.* **2016**, *28*, 2888–2895; b) R. Zhang, S. Wen, N. Wang, K. Qin, E. Liu, C. Shi, N. Zhao, *Adv. Energy Mater.* **2018**, *8*, 1800914; c) Q. Yun, Y. B. He, W. Lv, Y. Zhao, B. Li, F. Kang, Q. H. Yang, *Adv. Mater.* **2016**, *28*, 6932–6939; d) Z. Peng, N. Zhao, Z. Zhang, H. Wan, H. Lin, M. Liu, C. Shen, H. He, X. Guo, J.-G. Zhang, *Nano Energy* **2017**, *39*, 662–672; e) H. Ye, S. Xin, Y.-X. Yin, J.-Y. Li, Y.-G. Guo, L.-J. Wan, *J. Am. Chem. Soc.* **2017**, *139*, 5916–5922; f) S. Liu, A. Wang, Q. Li, J. Wu, K. Chiou, J. Huang, J. Luo, *Joule* **2018**, *2*, 184–193; g) X. Q. Zhang, X. Chen, X. B. Cheng, B. Q. Li, X. Shen, C. Yan, J. Q. Huang, Q. Zhang, *Angew. Chem. Int. Ed.* **2018**, *57*, 5301–5305; *Angew. Chem.* **2018**, *130*, 5399–5403; h) X. Fan, L. Chen, O. Borodin, X. Ji, J. Chen, S. Hou, T. Deng, J. Zheng, C. Yang, S. C. Liou, K. Amine, K. Xu, C. Wang, *Nat. Commun.* **2018**, *13*, 715–722; i) H.-K. Kang, S.-G. Woo, J.-H. Kim, S.-R. Lee, D.-G. Lee, J.-S. Yu, *J. Power Sources* **2019**, *413*, 467–475; j) Q. Pang, X. Liang, I. R. Kochetkov, P. Hartmann, L. F. Nazar, *Angew. Chem. Int. Ed.* **2018**, *57*, 9795–9798; *Angew. Chem.* **2018**, *130*, 9943–9946.
- [15] a) W. Zhang, H. L. Zhuang, L. Fan, L. Gao, Y. Lu, *Sci. Adv.* **2018**, *4*, eaar4410; b) A. M. Hafez, Y. Jiao, J. Shi, Y. Ma, D. Cao, Y. Liu, H. Zhu, *Adv. Mater.* **2018**, *30*, 1802156; c) J. Zhao, G. Zhou, K. Yan, J. Xie, Y. Li, L. Liao, Y. Jin, K. Liu, P.-C. Hsu, J. Wang, *Nat. Nanotechnol.* **2017**, *12*, 993.
- [16] R. Mukherjee, A. V. Thomas, D. Datta, E. Singh, J. Li, O. Eksik, V. B. Shenoy, N. Koratkar, *Nat. Commun.* **2014**, *5*, 3710.
- [17] W. Liu, Y. Xia, W. Wang, Y. Wang, J. Jin, Y. Chen, E. Paek, D. Mitlin, *Adv. Energy Mater.* **2019**, *9*, 1802918.
- [18] a) A. Basile, A. I. Bhatt, A. P. O'Mullane, *Nat. Commun.* **2016**, *7*, 11794; b) S. Liu, X. Xia, S. Deng, L. Zhang, Y. Li, J. Wu, X. Wang, J. Tu, *Energy Storage Mater.* **2018**, *15*, 31–36.
- [19] a) L.-L. Lu, J. Ge, J.-N. Yang, S.-M. Chen, H.-B. Yao, F. Zhou, S.-H. Yu, *Nano Lett.* **2016**, *16*, 4431–4437; b) T. T. Zuo, X. W. Wu, C. P. Yang, Y. X. Yin, H. Ye, N. W. Li, Y. G. Guo, *Adv. Mater.* **2017**, *29*, 1700389.
- [20] M. Bai, K. Xie, K. Yuan, K. Zhang, N. Li, C. Shen, Y. Lai, R. Vajtai, P. Ajayan, B. Wei, *Adv. Mater.* **2018**, *30*, 1801213.
- [21] Z. Liang, D. Lin, J. Zhao, Z. Lu, Y. Liu, C. Liu, Y. Lu, H. Wang, K. Yan, X. Tao, *Proc. Natl. Acad. Sci. USA* **2016**, *113*, 2862–2867.
- [22] L. Liu, Y.-X. Yin, J.-Y. Li, N.-W. Li, X.-X. Zeng, H. Ye, Y.-G. Guo, L.-J. Wan, *Joule* **2017**, *1*, 563–575.

Manuscript received: March 24, 2020  
Accepted manuscript online: March 31, 2020  
Version of record online: May 18, 2020